We are IntechOpen, the world's leading publisher of Open Access books Built by scientists, for scientists

4,800
Open access books available

122,000
International authors and editors

135M
Downloads

Our authors are among the

154
Countries delivered to

TOP 1%
most cited scientists

12.2%
Contributors from top 500 universities

WEB OF SCIENCE™

Selection of our books indexed in the Book Citation Index in Web of Science™ Core Collection (BKCI)

Interested in publishing with us?
Contact book.department@intechopen.com

Numbers displayed above are based on latest data collected.
For more information visit www.intechopen.com

12

Propagation of Electromagnetic Waves in Thin Dielectric and Metallic Films

Luc Lévesque
Royal Military College of Canada
Canada

1. Introduction

Matrix formalism is a very systematic method to find the reflectance or transmittance in a stratified medium consisting of a pile of thin homogeneous films. Fitting experimental values of reflectance curve to expressions obtained from the matrix formalism method is an efficient method to estimate the refractive index (n) of a dielectric and/or the real and imaginary parts of a metal permittivity (ε). In the next section, the method of matrix formalism is briefly reviewed with some examples to show how it can be applied in curve fitting to determine refractive indices or the metal permittivity. Applications to more complex structures such as planar waveguides and periodic grating are presented in sections 2 and 3, respectively.

1.1 Matrix formalism for the transverse electric and magnetic waves in stratified thin films

Maxwell equations will be applied at each interface between two homogeneous media to find the characteristic matrix defining a thin film. Let us consider figure 1 for a transverse electric (TE) wave with the E-field vector perpendicular to the plane of incidence for one thin homogeneous film.

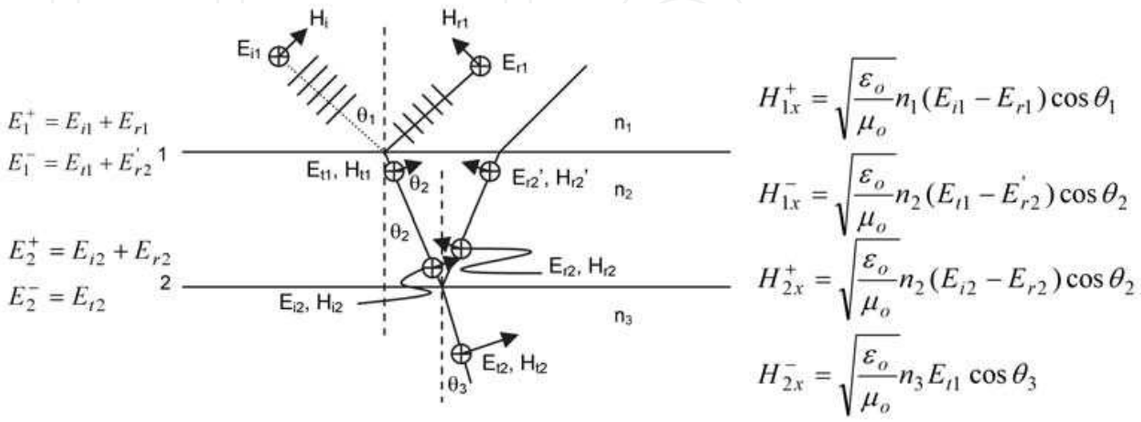

Fig. 1. Electric field (E) and magnetic field (H) in each medium of refractive index n_1, n_2 and n_3.

In figure 1, the H-field is related to the E-field using:

$$H_{i,r,t} = \sqrt{\frac{\varepsilon_o}{\mu_o}} n_{i,r,t} E_{i,r,t} \tag{1}$$

where ε_o and μ_o are referred to as the electric permittivity and the magnetic permeability, respectively. Letters i , r and t stand for incident, reflected and transmitted rays, respectively and the homogeneous medium is identified using numbers 1, 2 or 3.
As both the E and H fields are continuous at boundary 1, one may write E_1 and H_1 as:

$$E_1 = E_1^- = E_{t1} + E_{r2}^{'} \tag{2}$$

$$H_{1x} = H_{1x}^- = n_2 \sqrt{\frac{\varepsilon_o}{\mu_o}} (E_{t1} - E_{r2}^{'}) \cos\theta_2 = Y_2 (E_{t1} - E_{r2}^{'}) \tag{3}$$

where

$$Y_2 = n_2 \sqrt{\frac{\varepsilon_o}{\mu_o}} \cos\theta_2 \tag{4}$$

The system of equations (2) and (3) can be written under the matrix form as:

$$\begin{bmatrix} E_1 \\ H_{1x} \end{bmatrix} = \begin{bmatrix} 1 & 1 \\ Y_2 & -Y_2 \end{bmatrix} \begin{bmatrix} E_{t1} \\ E_{r2}^{'} \end{bmatrix} \tag{5}$$

At interface 2, we merely write

$$E_2 = E_2^+ = E_{i2} + E_{r2} \tag{6}$$

By making use of the E-field amplitude phase shift, it can be shown that E_{i2} and E'_{r2} can be expressed as:

$$E_{i2} = E_{t1} e^{-jk_2 h_2} \tag{7}$$

and

$$E_{r2}^{'} = E_{r2} e^{-jk_2 h_2} \tag{8}$$

respectively, with

$$h_2 = d_2 \cos\theta_2 \tag{9}$$

where d_2 is the thickness of the homogenous thin film and θ_{i2} is the angle defined as shown in figure 1. k_2 is the wave-vector in the thin homogeneous film (medium 2) , which is given as

$$k_2 = \frac{2\pi}{\lambda} n_2 \tag{10}$$

where λ is the wavelength of the monochromatic incident light when propagating in a vacuum.

Equations (7) and (8) are used to express the tangential component of the H-field vector at interface 2 as:

$$H_{2x} = Y_2(E_{t1}e^{-jk_2h_2} - E_{r2}^{'}e^{jk_2h_2}) \tag{11}$$

Using Equations (7) and (8), Equations (6) and (11) are expressed under the matrix form and by matrix inversion one can show that:

$$\begin{bmatrix} E_{t1} \\ E_{r2}^{'} \end{bmatrix} = \begin{bmatrix} e^{jk_2h_2}/2 & e^{jk_2h_2}/2Y_2 \\ e^{-jk_2h_2}/2 & -e^{-jk_2h_2}/2Y_2 \end{bmatrix} \begin{bmatrix} E_2 \\ H_{2x} \end{bmatrix} \tag{12}$$

Lastly, substituting Equation (12) into Equation (5) the E and H field components at interface 1 are related to those at interface 2 by:

$$\begin{bmatrix} E_1 \\ H_{1x} \end{bmatrix} = \begin{bmatrix} \cos(k_2h_2) & j\sin(k_2h_2)/Y_2 \\ jY_2\sin(k_2h_2) & \cos(k_2h_2) \end{bmatrix} \begin{bmatrix} E_2 \\ H_{2x} \end{bmatrix} = M_2 \begin{bmatrix} E_2 \\ H_{2x} \end{bmatrix} \tag{13}$$

The 2x2 matrix in equation (13) is the characteristic matrix (M_2) of the homogenous thin film. Note that M_2 is unimodular as its determinant is equal to 1. Assuming another film lying just underneath the thin film shown in figure 1, from Equation (13) we imply that field components E and H at interface 2 will be related to those at interface 3 by the matrix equation:

$$\begin{bmatrix} E_2 \\ H_{2x} \end{bmatrix} = \begin{bmatrix} \cos(k_3h_3) & j\sin(k_3h_3)/Y_3 \\ jY_3\sin(k_3h_3) & \cos(k_3h_3) \end{bmatrix} \begin{bmatrix} E_3 \\ H_{3x} \end{bmatrix} = M_3 \begin{bmatrix} E_3 \\ H_{3x} \end{bmatrix} \tag{14}$$

Substituting Equation (14) into Equation (13) one finds:

$$\begin{bmatrix} E_1 \\ H_{1x} \end{bmatrix} = M_2M_3 \begin{bmatrix} E_3 \\ H_{3x} \end{bmatrix} \tag{15}$$

By applying this method repeatedly for a stratified system of N thin homogeneous thin films we can write:

$$\begin{bmatrix} E_1 \\ H_{1x} \end{bmatrix} = M_2M_3...M_N \begin{bmatrix} E_N \\ E_{Nx} \end{bmatrix} = M \begin{bmatrix} E_N \\ E_{Nx} \end{bmatrix} \tag{16}$$

where $Y_l = \sqrt{\frac{\varepsilon_o}{\mu_0}} n_l \cos\theta_l$, $k_l = \frac{2\pi}{\lambda} n_l$ and $h_l = d_l \cos\theta_l$ for interfaces l = 2,3, … , N. (Born & Wolf, 1980) show that the reflection and transmission coefficient amplitudes for a system of N-1 layers (l = 2 to N) lying on a substrate of refractive index n_s can be expressed from the matrix entries of the system matrix M as:

$$r_{\perp} = \frac{E_{i1}}{E_{r1}} = \frac{Y_1m_{11} + Y_oY_sm_{12} - m_{21} - Y_sm_{22}}{Y_1m_{11} + Y_oY_sm_{12} + m_{21} + Y_sm_{22}} \tag{17}$$

where $r_{\perp}$ is referred to as the reflection coefficient for the TE wave. Admittances Y_1 and Y_s for the incident medium and the substrate hosting the system of N-1 homogeneous thin films are given by:

$$Y_1 = \sqrt{\frac{\varepsilon_o}{\mu_o}} n_1 \cos\theta_1 \tag{18}$$

and

$$Y_s = \sqrt{\frac{\varepsilon_o}{\mu_o}} n_s \cos\theta_N \tag{19}$$

For the case where the H-field is perpendicular to the plane of incidence (TM wave), the impedances Y_1, Y_l *and* Y_s must be replaced by Z_1 , Z_l and Z_s , which are given by

$$Z_1 = \sqrt{\frac{\mu_o}{\varepsilon_o}} \frac{\cos\theta_1}{n_1} \tag{20}$$

$$Z_l = \sqrt{\frac{\mu_o}{\varepsilon_o}} \frac{\cos\theta_l}{n_l} \text{ for } l = 2,3,\ldots, \text{N-1} \tag{21}$$

and

$$Z_s = \sqrt{\frac{\mu_o}{\varepsilon_o}} \frac{\cos\theta_N}{n_s} \tag{22}$$

1.2 Examples with dielectrics and metal thin films with some experimental results

Expressions derived in the previous section can be applied to find the reflectance curve of thin dielectric or metal films. They can be applied to fit experimental reflectivity data points to determine refractive indices of a dielectric film or metal film relative permittivity and even their thickness. Before we illustrate how it is used, let us apply Equation (17) for the simple case of Fresnel reflection coefficient amplitude for an interface between two semi-infinite media.

1.2.1 Interface between two semi-infinite media (Fresnel reflection coefficient)

This situation can be mimicked by setting $d_2 = 0$ into Equation (13). In other words, interfaces 1 and 2 in Figure 1 collapse into one single interface separating two semi-infinite media of refractive index n_1 and n_2.

Characteristic matrix in Equation (13) can be used to find the matrix system for two semi-infinite media. Setting for $d_2 = 0$, the matrix system for the two semi-infinite media becomes the identity matrix as h_2 equals 0. This means that $m_{11} = m_{22} = 1$ and $m_{12} = m_{21} = 0$. Substituting the matrix entries into Equation (17) one obtains:

$$r_{\perp} = \frac{Y_1 - Y_s}{Y_1 + Y_s} = \frac{n_1 \cos\theta_1 - n_2 \cos\theta_2}{n_1 \cos\theta_1 + n_2 \cos\theta_2} \tag{23}$$

In the previous equation we use $n_s = n_2$ and $\theta_N = \theta_2$ for this single interface system. For the TM wave, it can be shown that:

$$r_{||} = \frac{Z_1 - Z_s}{Z_1 + Z_s} = \frac{n_2 \cos\theta_1 - n_1 \cos\theta_2}{n_2 \cos\theta_1 + n_1 \cos\theta_2} \tag{24}$$

We then retrieve the results for the Fresnel reflection coefficients. Results for the transmission coefficient amplitude (t) can be obtained in the same manner.

1.2.2 Reflectance curve for a thin metallic film of silver or gold (surface plasmons)

A matrix approach is used to compute the reflectance of a thin film coupled to the hypotenuse of a right angle prism. The system shown in Figure 2 can be modeled by using three characteristic matrices for the matching fluid, the glass slide, the metal film and then accounting for the various Fresnel reflection losses at both the entrance and output face of the prism.

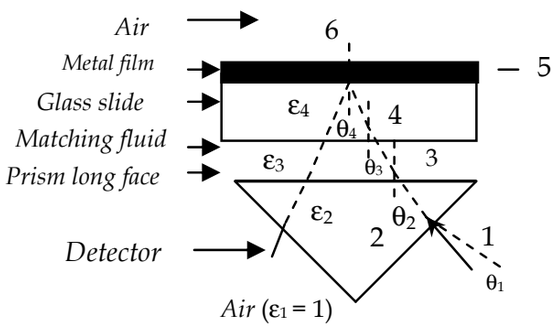

Fig. 2. Path of a laser beam propagating through all interfaces bounded by two given media. For a one way trip the media are (1) air, (2) glass, (3) matching fluid (greatly exaggerated), (4) glass (slide), (5) metal film (Au of Ag) and (6) air.

(Lévesque, 2011) expressed the characteristic matrix M of the sub-system of three layers in Figure 2 as

$$M = M_3 M_4 M_5 \tag{25}$$

where M_3, M_4 and M_5 are the characteristic matrices for the index matching fluid layer, the glass slide and the metal thin film, respectively. Each of these matrices is given by

$$M_i = \begin{bmatrix} \cos(\beta_i) & \frac{-i}{q_i}\sin(\beta_i) \\ -iq_i \sin(\beta_i) & \cos(\beta_i) \end{bmatrix} \tag{26}$$

where i =3, 4 or 5. β_i and q_i for p-polarized light are expressed as

$$\beta_i = \frac{2\pi}{\lambda} n_i d_i \cos\theta_i \tag{27}$$

$$q_i = \sqrt{\frac{\mu_o}{\varepsilon_o}}\sqrt{\frac{1}{\varepsilon_i}}\cos\theta_i = \sqrt{\frac{\mu_o}{\varepsilon_o}}q_i^{'} \tag{28}$$

respectively, where $\boldsymbol{\varepsilon_I}$ (= n_i^2) is the relative permittivity of the material. Using Snell's law, note that

$$\cos\theta_i = \left(1 - \frac{\varepsilon_2 \sin^2\theta_2}{\varepsilon_i}\right)^{1/2} \tag{29}$$

We are assuming all media to be non-magnetic and d_3, d_4 and d_5 are the thicknesses of the matching fluid, glass slide and the metal film, respectively. ε_3, ε_4 and ε_5 (= $\varepsilon'_5 + i\varepsilon_5''$) are the relative permittivity for the matching fluid, the glass slide and the metal film, respectively. ε_5' and ε_5'' are respectively, the real and imaginary parts of the metal film relative permittivity. By taking into account the Fresnel reflection losses F_1 at the input and output faces of the glass prism, the reflectance for the p-polarized light R_{Det} is given by:

$$R_{Det} = F_1\left|\frac{(m_{11} + m_{12}q_6^{'})q_1^{'} - (m_{21} + m_{22}q_6^{'})}{(m_{11} + m_{12}q_6^{'})q_1^{'} + (m_{21} + m_{22}q_6^{'})}\right|^2 \tag{30}$$

where m_{ij} are the entries of matrix M and F_1 is given by

$$F_1 = \left[\frac{4n_2\cos\theta_1\cos\theta_2}{(\cos\theta_2 + n_2\cos\theta_1)^2}\right]^2 \tag{31}$$

In previous equation n_2 is the refractive index of the prism. Investigations on optical reflectivity were done on glass slides which were sputtered with gold or silver. These glass slides were pressed against a right angle prism long face and a physical contact was then established with a refractive index matching fluid. The prism is positioned on a rotary stage and a detector is measuring the signal of the reflected beam after minute prism rotations of roughly 0.03°. The p-polarized light at λ = 632.8 nm is incident from one side of a glass prism and reflects upon thin metal films as shown in figure 3. As exp (-jωt) was assumed in previous sections, all complex permittivity ε must be expressed as $\varepsilon = \varepsilon' + j\varepsilon''$.

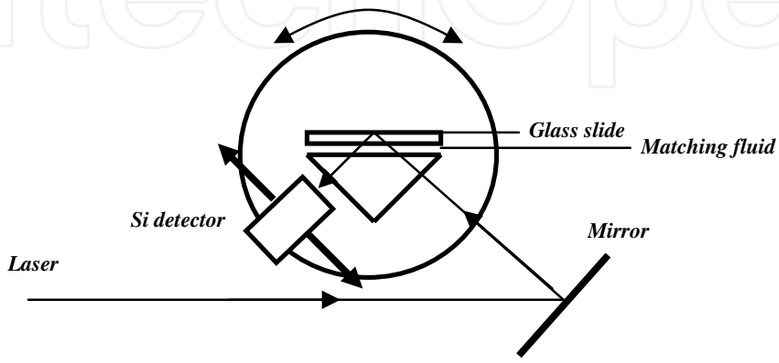

Fig. 3. Experimental set-up to obtain reflectivity data points.

If no film is coating the glass slide, a very sharp increase in reflectivity is expected when θ_4 approaches the critical angle. This sudden increase would occur at $\theta_c = \sin^{-1}(1/n_2) \sim 41.3^o$. The main feature of the sharp increase in the reflectivity curve is still obvious in the case of a metalized film. This is so as the penetration of the evanescent field is large enough to feel the presence of air bounding the thin metal film. As silver or gold relative permittivity (optical constant) is complex, $\cos\theta_5$ becomes complex in general and as a result θ_5 is not represented in Fig. 2. This means physically that the field penetrates into the metal film and decays exponentially through the film thickness. At an optimum thickness, the evanescent field excites charge oscillations collectively at the metal-film-air surface (c.f.fig.2), which is often used to probe the metal surface. This phenomenon known as Surface Plasmon Resonance (Raether, 1988; Robertson & Fullerton, 1989; Welford, 1991) is occurring at an angle of θ_2 that is a few degrees greater than θ_c. For a He-Ne laser beam at λ = 632.8 nm, that is incident from the prism's side (c.f.fig.2) and then reflecting on silver or gold metal films, surface plasmons (SP) are excited at θ_2 near 43° and 44°, respectively. At these angles, the incident light wave vector matches that of the SP wave vector. At this matching condition, the incident energy delivered by the laser beam excites SP and as a result of energy conservation the reflected beam reaches a very low value. At an optimal thickness, the reflectance curve displays a very sharp reflectivity dip. Figure 4 shows the sudden increase at the critical angle followed by a sharp dip in the reflectance curve in the case of a gold film of various thicknesses, which is overlaying the glass slide.

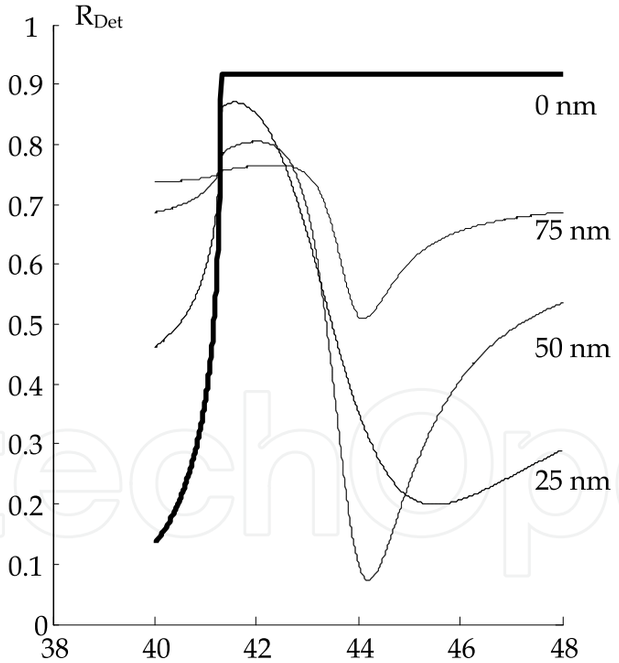

Fig. 4. Reflectance curves for gold films of various thicknesses d_5 obtained from Eq.(30). We used d_3 = 10000 nm and d_4 = 1000000 nm (1mm), n_2 =1.515, n_3 =1.51, n_4 =1.515 and ε_5 = -11.3+3j.

Reflectance curves for gold films sputtered on glass slides show a sudden rise at the critical angle θ_c followed by a sharp drop reaching a minimum near 44°. For all film thicknesses, a sudden rise occurs at the critical angle. Note that the reflectance curve for a bare glass slide

(d_5 = 0 nm) is also shown in figure 4. At smaller thicknesses, the electromagnetic field is less confined within the metallic film and does penetrate much more into the air. The penetration depth of the electromagnetic field just before reaching the critical angle ($\theta < 41.3^o$) is indicated by a lower reflectance as d_5 gets closer to zero, as shown in Fig.4. The reflectivity drop beyond θ_c is known as Surface Plasmon Resonance (SPR). SPR is discussed extensively in the literature and is also used in many applications. Good fitting of both regions displaying large optical intensity change is also useful in chemical sensing devices. As a result fitting of both regions is attempted using the exact function curve without any approximations given by Eq. (30). Eq. (30) is only valid for incident plane wave. Therefore, the reflectivity data points were obtained for a very well-collimated incident laser beam. A beam that is slightly converging would cause more discrepancy between the curve produced from Eq. (30) and the reflectivity data points. Although the Fresnel loss at the transparent matching fluid-glass slide interface is very small, it was taken into account in Eq. (30), using d_3=10 000nm (10 μm) in matrix M_3. The theoretical reflectance curve is not affected much by the matching fluid thickness d_3. It was found that d_3 exceeding 50 μm produces larger oscillations in the reflectance curve predicted by Eq.(30). As the oscillations are not noticeable amongst the experimental data points, the value of d_3 = 10 μm was deemed to be reasonable. A function curve from Eq. (30) is generated by changing three output parameters ε_5', ε_5'' and d_5. The sum of the squared differences (SSQ) between R_{Det} and the experimental data points R_i is calculated. The best fit is determined when the SSQ is reaching a minimum. The SSQ is defined as:

$$SSQ = \sum_{i=1}^{N} (R_i - R_{Det})^2 \tag{32}$$

where i is a subscript for each of the N data points from the data acquisition. Each sample was placed on a rotary stage as shown in Figure 3 and a moving Si-pin diode is rotating to track down the reflected beam to measure a DC signal as a function of θ_2. The reflectivity data points and typical fits are shown in Figure 5.

In the fit in Fig. 5a, we used $n_2 = n_4 = 1.515$, $n_3 = 1.47$(glycerol) for red light, d_3 = 10 000 nm, ε_5 =-11.55+3.132j and d_5 =43.34 nm.

In the fit in Fig. 5b, we used $n_2 = n_4 = 1.515$, $n_3 = 1.47$(glycerol) for red light, d_3 = 10 000 nm, ε_5 = -10.38+2.22j and d_5 = 53.8 nm. The three output parameters (ε_5', ε_5'' and d_5) minimizing the SSQ determine the best fit. Plotting the SSQ in 3D as a function of ε_5' and d_5 at ε_5'' = 3.132 shows there is indeed a minimum in the SSQ for the fit shown in Fig.5a. Figure 6 shows a 3D plot of the SSQ near the output parameters that produced (Lévesque, 2011) the best fit in Fig. 5a. 3D plots at values slightly different from ε_5'' = 3.132 yield larger values for the minimum.

2. Wave propagation in a dielectric waveguide

In this section, we apply the matrix formalism to a dielectric waveguide. We will describe how the reflectance curve changes for a system such as the one depicted in Fig. 2 if a dielectric film is overlaying the metal film. It will be shown that waveguide modes can be excited in a dielectric thin film overlaying a metal such as silver or gold and that waveguide modes supported by the dielectric film depend upon its thickness.

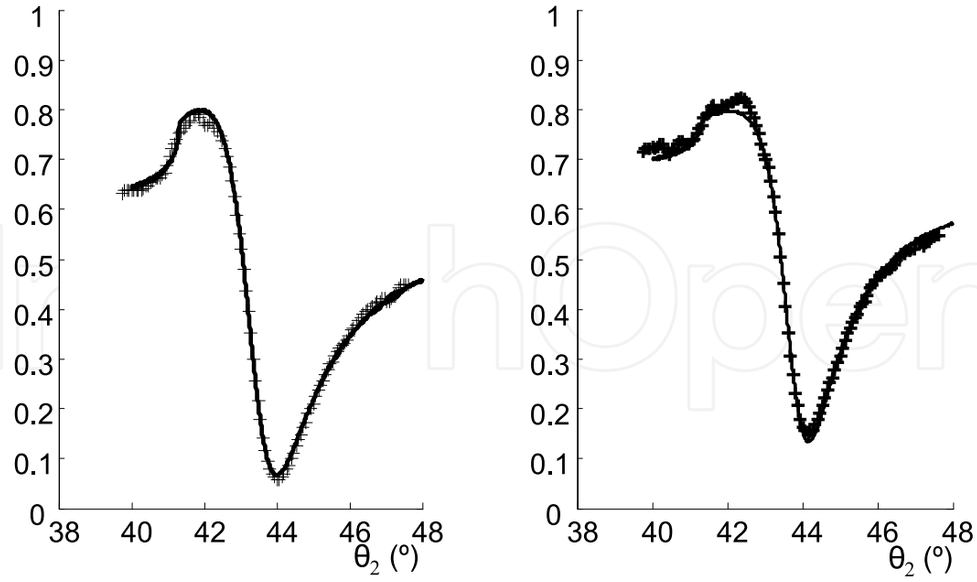

Fig. 5. Reflectivity data points (+) and a fit (solid line) produced from Eq.(30) for two different gold films.

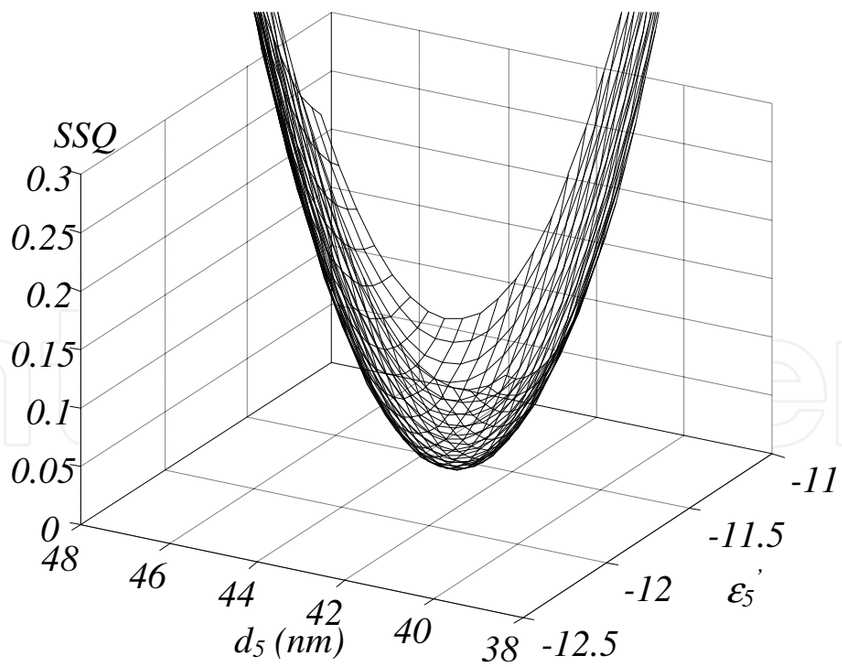

Fig. 6. 3D plot of SSQ as a function of two output parameters at a given value of ε_5''(= 3.132). We assumed the glycerol layer (d_3) to be 10 μm and the thickness of the glass slide is 1 mm (d_4). The SSQ reaches a minimum of 0.01298 for ε_5' =-11.55, ε_5'' = 3.132 and d_5 =43.34 nm.

2.1 Wave propagation in dielectric films

Let us consider a dielectric film of thickness d_6 overlaying the metal film in Figure 2. We will be assuming that the top surface of the overlaying dielectric is bounded by the semi-infinite air medium. The characteristic matrix M for the sub-system of four layers can be expressed as:

$$M = M_3 M_4 M_5 M_6 \tag{33}$$

where M_3, M_4, M_5 and M_6 are the characteristic matrices for the index matching fluid layer, the glass slide, the metal thin film and the thin dielectric film, respectively. Each matrix in Eq.(33) is given by Eq.(26) for i = 3,4,5 and 6 and the reflectance for the p-polarized wave is given by Eq.(30). For this four layer system, q_6' in Eq.(30) should be replaced by q_7' (air) and m_{11}, m_{12}, m_{21} and m_{22} are the entries of the system matrix given by Eq.(33). The expression for q_6 is given by Eq.(28) and is used in the computation of M_6 for the dielectric film characteristic matrix.

2.1.1 Computation of reflectance with a thin dielectric film and experimental results

Eq. (30) can be used with the minor modifications discussed in section 2.1 to find the reflectance of the system in Fig. 2 with an extra dielectric film processed on the metal film. The dielectric film can support waveguide modes if the laser beam is directed at very precise incident angle θ_2. Let us consider a transparent polymer film with a real permittivity $\varepsilon_6 = 2.30$ processed on a silver film. The computation is done for a silver film that is 50 nm thick. Silver permittivity is assumed to be $\varepsilon_5 = -18.0 + 0.6i$ and the prism refractive index to be 2.15 (ZrO_2) for He-Ne laser at $\lambda = 632.8$ nm. We also assume that the metal film is directly coated on the prism long face and as a result we set $d_3 = d_4 = 0$. In other words M_3 and M_4 are expressed by identity matrices. Figure 7 is showing the reflectance curve for a dielectric film of different thickness that is overlaying the silver film coated on the high refractive index ZrO_2 prism.

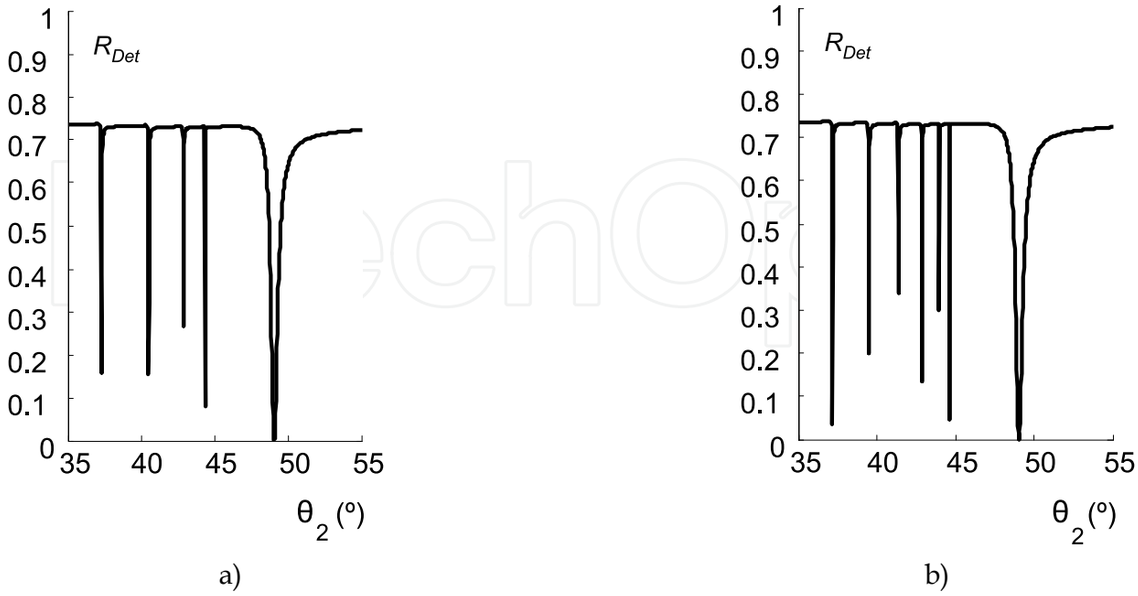

Fig. 7. a) Reflectance curve for a lossless dielectric film of 1.7 μm overlaying a thin silver film
b) Reflectance curve for a lossless dielectric film of 2.5 μm overlaying a thin silver film

In figure 7a, a series of very sharp reflectivity drops occur in the reflectance curve for θ_2 within the range 35°-45°. These sharp reflectivity drops with small full width at half maximum (FWHM) are waveguide modes supported by the dielectric film. The last reflectivity dip with a larger FWHM near $\theta_2 \sim 50°$ is due to surface plasmon resonance (SPR) and is mostly depending upon the metal film properties and its thickness as discussed in section 1.2.2. A thicker dielectric film (c.f. fig. 7b) can support more waveguide modes and as a result the number of sharp reflectivity dip for θ_2 within the range 35° to 45° is expected to be greater. Note that the FWHM of the SPR dip remains at the same position as the metal film thickness was not changed. These waveguide modes do not propagate a very large distance as light is slightly attenuated when reflecting at the metal-dielectric film interface. Therefore, at precise angle θ_2 the incident light is probing the dielectric film locally before being reflected by the thin metal film. Nevertheless, the laser beam is simultaneously probing the metal and the dielectric films because it creates SPR on the thin metal film and waveguide modes are being supported by the dielectric film. In practice, dielectric films are not lossless (Podgorsek & Franke, 2002) and their permittivity should be expressed using a small imaginary part. Let us assume that each dielectric films in Fig. 7 have a permittivity of $\varepsilon_6 = 2.30 + 0.005j$.

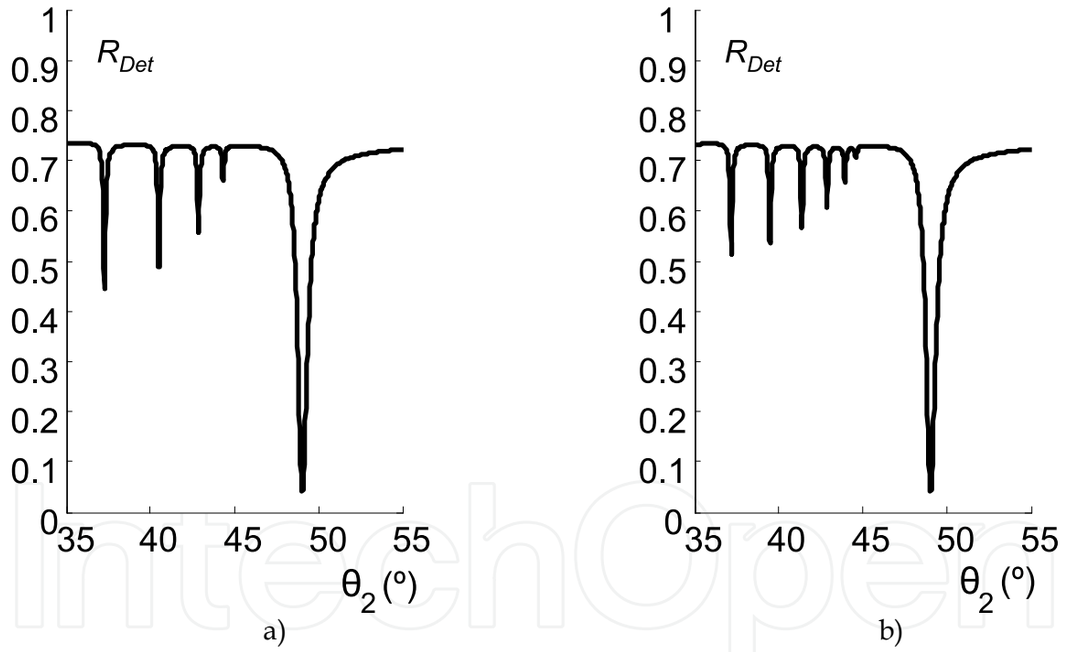

Fig. 8. a) Reflectance curve for a dielectric film ($\varepsilon_6 = 2.30 + 0.005j$, $d_6 = 1.7$ μm) overlaying the metal film. b) Reflectance curve for a dielectric film ($\varepsilon_6 = 2.30 + 0.005j$, $d_6 = 2.5$ μm) overlaying the metal film.

Note from figures 7 and 8 that the waveguide mode dips are greatly attenuated when a small imaginary part is assumed in the dielectric film permittivity. The dips at larger angles (near 45°) are getting smaller as the propagation distance into in the dielectric film is larger as θ_2 increases. Note that the SPR dip is not much affected by the imaginary part of ε_6. Essentially, the whole 4-layer system of prism material-silver film- dielectric film-air can be mounted on a rotary stage and the angle θ_2 can be varied using a set-up similar to that

shown in figure 3. As it is difficult to obtain a large dynamic range in the measurements of reflectivity data points, scans must be done successively to cover a long range of incident angle. Figure 9 shows reflectance curves for a transparent layer of polyimide processed directly on silver films. Ranges of incident angle θ_2 where no noticeable change in reflectivity were observed are not shown. Only the dips in the reflectivity data points are fitted by Eq. (30).

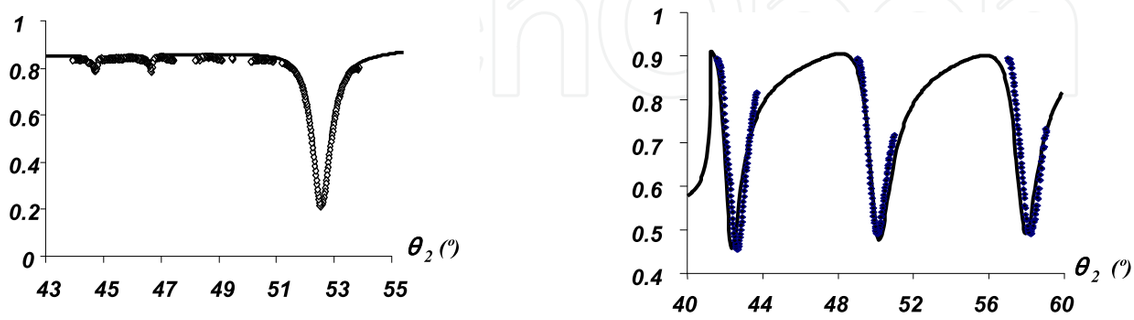

a) b)

Fig. 9. Reflectivity data points of the 4-layer system and fits (solid lines) from Eq. (30) for a) ZrO_2 prism-Ag-polyimide film b) glass prism-Ag-polyimide film

Using a method based on the optimization of the sum of square (SSQ) as presented in section 1.2.2, thicknesses and the complex permittivities of both films can be estimated. Values obtained from the minimization of the SSQ are given in table 1. Uncertainties are estimated from a method described by (Lévesque et al., 1994).

Prism	*ZrO2*	*Glass*
ε_5' *(Ag)*	*-17.41±0.10*	*-18.1 ±0.1*
ε_5'' *(Ag)*	*0.2 ±0.1*	*1.36 ±0.08*
d_5	*615 ±15Å*	*146 ±5Å*
ε_6' *(Pi)*	*2.495±0.001*	*2.230±0.002*
ε_6'' *(Pi)*	*0.011±0.003*	*0.0017±0.0002*
d_6	*1.488±0.004µm*	*1.723±0.003µm*

Table 1. Thicknesses and permittivities of the silver (Ag) and polyimide (*P*i) films.

3. Diffraction efficiency (DE) in dielectric periodic grating structures

Abrupt changes in reflectivity or transmission were first observed in gratings as early as 1902 (Wood, 1902). These so-called anomalies in diffraction efficiency (DE) occurring over an angle range or a wavelength spectrum are very different from the normally smooth diffraction curves. These abrupt changes in DE led researchers to design and investigate resonant filters for applications in many devices including gratings.

Rigorous coupled wave analysis (RCWA) has been used extensively (Moharam et al., 1995; Lalanne & Morris, 1996; Lenaerts et al., 2005) to calculate diffraction efficiencies (DE) in waveguide structures. The application of RCWA to resonant-grating systems has been

investigated mostly for both the *TE* and *TM* polarization. In this section, the basic binary dielectric rectangular-groove grating is treated with careful considerations on the computation of DE. The results obtained for binary dielectric rectangular-groove grating are also applied to metallic grating. Introduction to photonic bandgap systems are discussed and some examples are presented at the end of this section.

3.1 Theory of coupled wave analysis

As the numerical *RCWA* method is introduced extensively in the literature, only the basics equations will be presented in this section. Computation will be done for the *TM* wave on ridge binary grating bounded by two semi-infinite dielectric media of real permittivities ε_1 and ε_3. The type of structures presented in this section is depicted in figure 10.

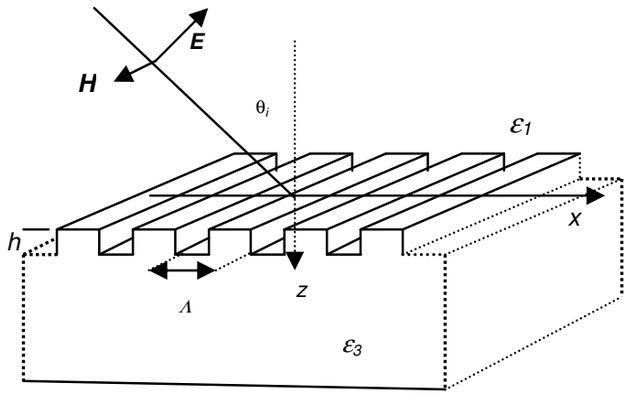

Fig. 10. Basic structure of the binary rectangular-groove grating bounded by two semi-infinite dielectrics.

The relative permittivity $\varepsilon(x)$ of the modulated region shown in figure 10 is varying periodically along the x-direction and is defined as:

$$\varepsilon(x) = \sum_s \varepsilon_s \exp(-2\pi jsx / \Lambda) \tag{34}$$

where ε_s is the sth Fourier component of the relative permittivity in the grating region (0< z <h), which can be complex in the case of metallic gratings. The incident normalized magnetic field that is normal to the plane of incidence (*cf. fig.10*) is given by:

$$H_{inc,y} = \exp[-jk_o n_1(\sin\theta_i x + \cos\theta_i z)] \tag{35}$$

where $k_o = 2\pi/\lambda$. θ_i is the incident angle with respect to the z-axis as shown in figure 10. The normalized solutions in regions 1 ($z < 0$) and 3 ($z > h$) are expressed as:

$$H_{1,y} = H_{inc,y} + \sum_i R_i \exp[-j(k_{xi}x - k_{1,zi}z)] \tag{36}$$

$$H_{3,y} = \sum_i T_i \exp[-j(k_{xi}x + k_{3,zi}(z-h))] \tag{37}$$

where k_{xi} is defined by the Floquet condition, i.e.,

$$k_{xi} = k_o(n_1 \sin\theta_i - i(\lambda / \Lambda)) \tag{38}$$

In previous equations, Λ is the grating spacing, n_1 ($\equiv \sqrt{\varepsilon_1}$) is the refractive index of medium 1 and

$$k_{l,zi} = \begin{cases} k_o\left[n_l^2 - \left(\frac{k_{xi}}{k_o}\right)^2\right]^{1/2} & k_o n_l > k_{xi} \\ -jk_o\left[\left(\frac{k_{xi}}{k_o}\right)^2 - n_l^2\right]^{1/2} & k_{xi} > k_o n_l \end{cases} \tag{39}$$

with l = 1,3. n_3 ($\equiv \sqrt{\varepsilon_3}$) is the refractive index of medium 3.

R_i and T_i are the normalized electric-field amplitudes of the ith diffracted wave in media 1 and 3, respectively. In the grating region ($0 < z < h$) the tangential magnetic (y-component) and electric (x-component) fields of the *TM* wave may be expressed as a Fourier expansion:

$$\begin{aligned} H_y &= \sum_i U_{yi}(z)\exp(-jk_{xi}x) \\ E_x &= j(\frac{\mu_o}{\varepsilon_o})^{1/2}\sum_i S_{xi}(z)\exp(-jk_{xi}x) \end{aligned} \tag{40}$$

where U_{yi} (z) and S_{xi} (z) are the normalized amplitudes of the i^{th} space-harmonic which satisfy Maxwell's equations, i.e.,

$$\begin{aligned} \frac{\partial E_x}{\partial z} &= -j\omega\mu_o H_y + \frac{\partial E_z}{\partial x} \\ \frac{1}{\varepsilon(x)}\frac{\partial H_y}{\partial x} &= j\omega\varepsilon_o E_z \end{aligned} \tag{41}$$

where a temporal dependence of exp (jωt) is assumed ($j^2 = -1$) and ω is the angular optical frequency. ε_o and μ_o are respectively the permittivity and permeability of free space. As the exp (jωt) is used, all complex permittivity must be expressed under $\varepsilon = \varepsilon' - j\varepsilon''$.
Substituting the set of equations (40) into Maxwell's equations and eliminating E_z, the coupled-wave equations can be expressed in the matrix form as:

$$\begin{bmatrix} \partial U_y / \partial z' \\ \partial S_x / \partial z' \end{bmatrix} = \begin{bmatrix} 0 & E \\ B & 0 \end{bmatrix}\begin{bmatrix} U_y \\ S_x \end{bmatrix} \tag{42}$$

where z' equals $k_o z$.
Previous equations under the matrix form can be reduced to

$$\left[\partial^2 U_y / \partial z'^2\right] = [EB]\left[U_y\right] \tag{43}$$

where $B = K_x E^{-1} K_x - I$. E is the matrix formed by the permittivity elements, K_x is a diagonal matrix, with their diagonal entries being equal to k_{xm} / k_o and I is the identity matrix. The solutions of Eq. (43) and the set of Eq. (42) for the space harmonics of the tangential magnetic and electric fields in the grating region are expressed as:

$$U_{yi}(z) = \sum_{m=1}^{n} w_{i,m}(c_m^+ \exp[-jk_o q_m z] + c_m^- \exp[jk_o q_m (z-h)])$$
$$S_{xi}(z) = \sum_{m=1}^{n} v_{i,m}(-c_m^+ \exp[-jk_o q_m z] + c_m^- \exp[jk_o q_m (z-h)]) \tag{44}$$

where, $w_{,i,,m}$ and q_m are the elements of the eigenvector matrix W and the positive square root of the eigenvalues of matrix **G** (=-**EB**), respectively. The quantities c_m^+ and c_m^- are unknown constants (vectors) to be determined from the boundary conditions. The amplitudes of the diffracted fields R_i and T_i are calculated by matching the tangential electric and magnetic field components at the two boundaries. Using Eqs. (35) , (36), (44) and the previously defined matrices, the boundary conditions at the input boundary (z = 0) are:

$$\delta_{i,0} + R_i = Wc^+ + WXc^- \tag{45}$$

and

$$\frac{j\cos\theta}{n_1}\delta_{i,0} - jZ_1 R_i = Vc^+ - VXc^- \tag{46}$$

where X and Z_1 are diagonal matrices with diagonal elements $\exp(-jk_o q_m h)$ and $k_{1zi}/(n_1^2 k_o)$, respectively. c^+ and c^- are vectors of the diffracted amplitude in the i^{th} order. From (42) and (44), it can be shown that

$$V = jE^{-1}WQ \tag{47}$$

where $v_{m,l}$ are the elements of the product matrix with Q being a diagonal matrix with diagonal entries q_l.

At z = h, the boundary conditions are:

$$WXc^+ + Wc^- = T_i \tag{48}$$

and

$$VXc^+ - Vc^- = jZ_3 T_i \tag{49}$$

where Z_3 is the diagonal matrix with diagonal elements $k_{3zi}/(n_3^2 k_o)$. Multiplying each member of Eq. (48) by $-jZ_3$ and using Eq. (49) to eliminate T_i vectors c^- and c^+ are related by:

$$c^- = (jZ_3 W + V)^{-1}(-jZ_3 W + V)Xc^+ \tag{50}$$

Multiplying each member of Eq. (45) by jZ_1 and using Eq. (46) to eliminate R_i a numerical computation can be found for c^+ by making use of Eq.(50), that is:

$$c^{+} = C^{-1}(\frac{j\cos\theta}{n_1} + jZ_1)\delta_{i,o} \tag{51}$$

where

$$C = [(jZ_1W + V) + (jZ_1W - V)X(jZ_3W + V)^{-1}(-jZ_3W + V)X] \tag{52}$$

Note in Eq. (51) that $\delta_{i,0}$ is a column vector. In the case of a solution truncated to the first negative and positive orders,

$$\delta_{i,o} = \begin{bmatrix} 0 \\ 1 \\ 0 \end{bmatrix} \tag{53}$$

assuming the incident wave to be a plane wave. In this particular case

$$(\frac{j\cos\theta}{n_1} + jZ_1)\delta_{i,o} = \begin{bmatrix} 0 \\ j\frac{\cos\theta}{n1} + jZ_1(2,2) \\ 0 \end{bmatrix} \tag{54}$$

where $Z_1(2,2)$ is the element on line 2 and column 2 of matrix Z_1. Finally, the vector on the right-hand side of Eq.(54) is applied to the inverse matrix of C to find the column vector for the diffracted amplitude c^+ from Eq. (51). Then c^- is found from Eq. (50) and the normalized electric field amplitudes for R_i and T_i can be found from Eqs. (48) and (49).
Substituting Eq. (34) and Eq.(44) into Maxwell's equations and eliminating E_z , it can be shown that

$$\frac{\partial S_{xm}}{\partial z'} = j(\sum_p \frac{k_{xm}}{k_o}\varepsilon_{i-p}^{-1}\frac{k_{xm}}{k_o}U_{yp} - U_{yi}) \tag{55}$$

Eq. (55) is one of the two coupled-wave equations involving the inverse permittivity for the case of *TM* polarization only. In the conventional formulation (Wang et al., 1990; Magnusson & Wang, 1992; Tibuleac & Magnusson, 1997) the term ε_{i-p}^{-1} is treated by taking the inverse of the matrix *E* defined by the permittivity components (Moharam & Gaylord, 1981), with the *i*, *p* elements being equal to $\varepsilon_{(i-p)}$. In the reformulation of the eigenvalue problem (Lalanne & Morris, 1996), the term ε_{i-p}^{-1} is considered in a different manner by forming a matrix *A* of the inverse-permittivity coefficient harmonics for the two regions inside the modulated region. Fourier expansion in Eq.(34) is modified to:

$$1/\varepsilon(x) = \sum_s (1/\varepsilon)_s \exp(-2\pi jsx/\Lambda) \tag{56}$$

where $(1/\varepsilon)_s$ is the s^{th} Fourier component of the relative permittivity in the grating region.
Since the coupled-wave equations do not involve the inverse of the permittivity in the coupled-wave equations for the TE wave, matrix **A** is not needed in numerical computations

and the eigenvalue problem is greatly simplified in this case. As a result, solutions for the TE wave are more stable in metallic lamellar gratings.
Only the DE in reflection and transmission for zeroth order are computed in the examples that will be discussed throughout this section. The diffraction efficiencies in both reflection (DE_R) and transmission (DE_T) are defined as:

$$DE_R = R_0 R_0^* \mathrm{Re}(k_{1,z0} / (k_o n_1 \cos\theta_i)) \tag{57}$$

and

$$DE_T = T_0 T_0^* \mathrm{Re}(\frac{k_{3,z0}}{n_3^2}) / (\frac{k_o \cos\theta}{n_1}) \tag{58}$$

3.1.1 Examples with binary dielectric periodic gratings

Let us consider a binary rectangular-groove grating with real permittivity ε_L and ε_H as shown in figure 10. In the case of notch filters the higher permittivity value ε_H ($\Lambda / 2 < x < \Lambda$) is greater than ε_L ($0 < x < \Lambda / 2$). Figure 11 shows the numerical computation for *DE* from the RCWA formulation for the *TM* wave when only three orders (m = -1, 0, 1) are retained in the computation.

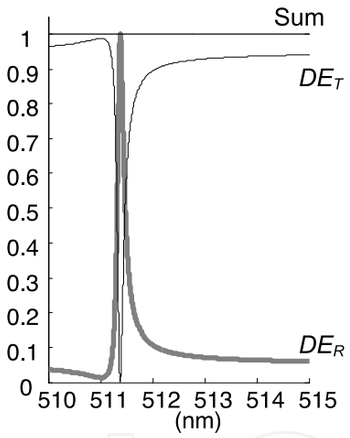

Fig. 11. DE_R and DE_T for a binary dielectric periodic grating for ε_L =4.00, ε_H = 4.41, Λ =314 nm, n_1 =1.00 (air), n_3 =1.52 (glass) and h = 134 nm.

From the principle of energy conservation, the sum of DE_R and DE_T must be equal to unity. This principle is useful to decide if the number of orders retained in the computation is sufficient. As no deviation from unity is seen in the sum of DE_R and DE_T in figure 11, three orders is deemed to be enough to describe the diffraction efficiencies within this narrow wavelength spectrum. At a wavelength of roughly 511.3 nm all the optical energy is reflected back in the opposite direction from that of the incident light. As a result, DE_T is reaching a zero value as destructive interferences occur within the grating at this precise wavelength value of 511.3 nm.

3.1.2 Examples with metallic periodic gratings

The theory presented in section 3.1 can be applied to metallic periodic gratings. For the TM wave many terms need to be retained in the calculation to reach convergence (Li &

Haggans, 1993). For the sake of saving time, a fairly accurate computation is reached after retaining ten orders when using the reformulated eigenvalue problem (Lalanne & Morris, 1996). Figure 12 shows DE_R for a metallic periodic grating using a 3D plot. Metallic periodic grating are used to excite surface plasmons (SP) to improve Surface-enhanced-Raman-Scattering (SERS) sensor performances (Sheng et al., 1982). At a given wavelength λ the reflectivity of the metallic grating should be symmetric with the incident angle θ. If a reflectivity drop occurs due to SP at θ, the metallic periodic grating should display a similar drop at -θ. Note that two minima occur on either side of normal incidence (θ = 0^o) and one single minimum is displayed at normal incidence for λ ~ 630 nm. Basically each minimum in DE_R forms two valleys which crisscross at normal incidence and λ ~ 630 nm. This point will become important in the next section where photonic band gap is discussed.

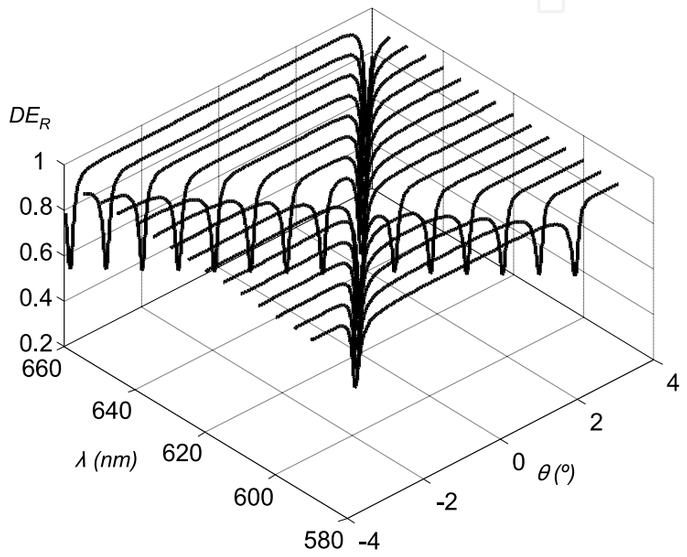

Fig. 12. 3D plot of DE_R for a periodic metallic grating. In the calculation, we used $n_1 = 1$, $\varepsilon_3 = \varepsilon_2 = -17.75 - 0.7j$, $\Lambda = 600$nm, $\varepsilon_L = -17.75 - 0.7j$, $\varepsilon_H = 1$, and h = 10.5 nm.

3.2 Photonic bandgap in metallic periodic gratings

Resonant surface plasmon (SP) coupling involving metallic periodic gratings has been extensively studied over the past years and more recently in work looking at photonic devices (Park et al., 2003; Barnes et al. 2003; Ebbesen et al., 1998; Ye & Zhang, 2004) surface-enhanced Raman scattering (Sheng et al., 1982) and photonic bandgaps (Barnes et al., 1996). Corrugated surfaces are commonly produced by direct exposure of a photoresist film to a holographic interference pattern. There is some experimental evidence that owing to nonlinear response of the photoresist, this technique leads to the presence of higher harmonics in addition to the fundamental pattern that is inscribed (Gallatin, 1987; Pai & Awada, 1991). The higher harmonics can then influence the propagation of the SP on the metallic periodic grating and, in particular, can generate a bandgap in the plasmon dispersion curve.

3.2.1 Generating a photonic bandgap with two metallic periodic gratings

Let us consider two metallic sinusoidal gratings with vectors K1 (= $2\pi/\Lambda 1$) and K2 (=$2\pi/\Lambda 2$) inscribed at the same location on the film surface. One grating acts as a coupler that allows light

to generate SPs while the second grating creates a bandgap in the dispersion curve for the SP propagation. Herein, we consider the case $K_2 = 2K_1$. More complicated cases such as $K_2 < 2K_1$ have also been investigated and may be found in the literature (Lévesque & Rochon , 2005).
The SP dispersion curve for a uniform silver or gold film in the absence of a gap is shown in Figure 13a and is described by:

$$k_{SP} = \frac{\omega}{c}\left(\frac{\varepsilon_m \varepsilon_d}{\varepsilon_m + \varepsilon_d}\right)^{1/2} \tag{59}$$

where k_{SP} is the wave vector of the SP modes coupled at the surface and ε_m and ε_d are the permittivities of the metal and dielectric material (air). The dispersion line for light incident at an angle θ and scattered by a vector K_1 is given by:

$$k_{light} = \frac{\omega}{c}\sin\theta \pm m_1 K_1 \tag{60}$$

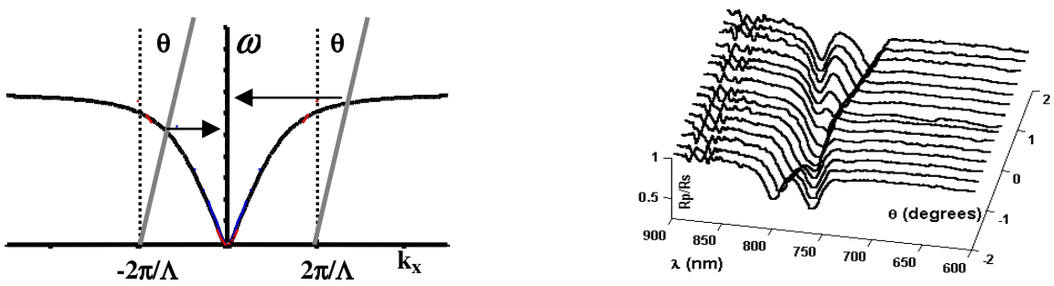

a) b)

Fig. 13. a) SP dispersion curves for one periodic grating of Bragg vector K_1 b) Normalized reflectance (R_p/R_s) curve for a single metallic grating with Λ ~ 755 nm.

Note from Figure 13a that at normal incidence (θ = 0°) SPs will be excited at a single wavelength from a loss or gain of light momentum by the grating Bragg vector $K_1 = 2\pi/\Lambda$. Scattering of incident light from the metallic grating at a given incident angle can fulfill the phase-matching condition ($k_{SP} = k_{light}$) for SP excitation. As θ increases from zero SPs can be generated if light scatters by a Bragg vector $\pm K_1$, i.e., two valleys will form for θ > 0° and θ < 0° as shown in Figure 13b. Experimentally, a fairly sharp dip in the reflectivity curve (R_p) was observed for the p-polarized light but not for the s-polarized light (R_s). To emphasize the SP contribution, the R_p reflectance curves were normalized to R_s in the range 600-900 nm spectral range. Curves shown in Figure 13b were predicted by DE_R computations shown in Figure 12.
The SP dispersion curves for the doubly corrugated surfaces and light lines are shown in Figure 14a.
It can be seen from Figure 14a) that two SPs can be generated at normal incidence as a bandgap is being created by the grating of Bragg vector K_2. As a result, SPs can be generated at $\omega = \omega_1$ and $\omega = \omega_2$. This means the band will open as shown in Figure 14b, where two minima are shown in the experimental data points for all incident angles (Lévesque & Rochon , 2005). Each of these minima corresponds to SP excitation at the air-metal grating surface when light is scattered by Bragg vector $\pm K_1$.

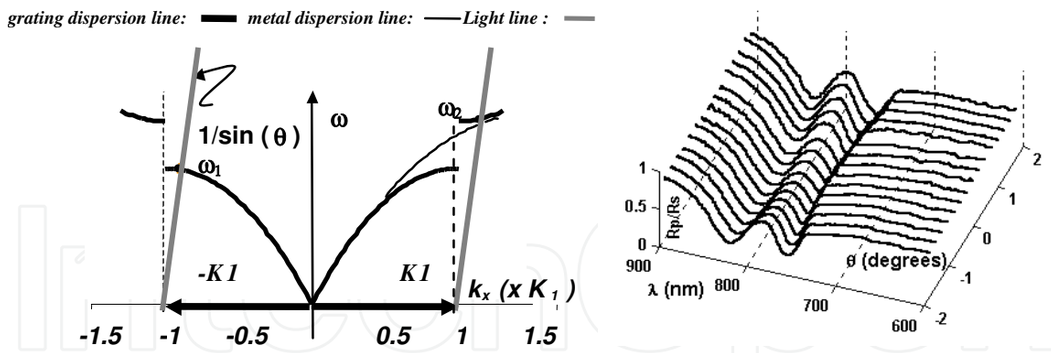

Fig. 14. a) SP dispersion curves for two superimposed periodic grating of Bragg vector K_1 and K_2 b) Normalized reflectance curve for a doubly corrugated surface with $\Lambda_1 \sim 755$ nm and $\Lambda_2 \sim 375$ nm.

3.2.2 Processing of the single and double metallic corrugated surfaces

Surface corrugations with selected pitches (Bragg vectors) can be produced on azopolymer films by direct exposure of an interference pattern from two coherent light beams at $\lambda = 532$ nm, as shown in Figure 15a. The two desired spacing are obtained by adjusting the angle φ (c. f fig.15a) between the writing beams, and their depth is determined by their exposure time. The films under investigation have two superimposed sinusoidal gratings with vectors K_1 and K_2. These azopolymer films were prepared on glass slides and then coated with a 50

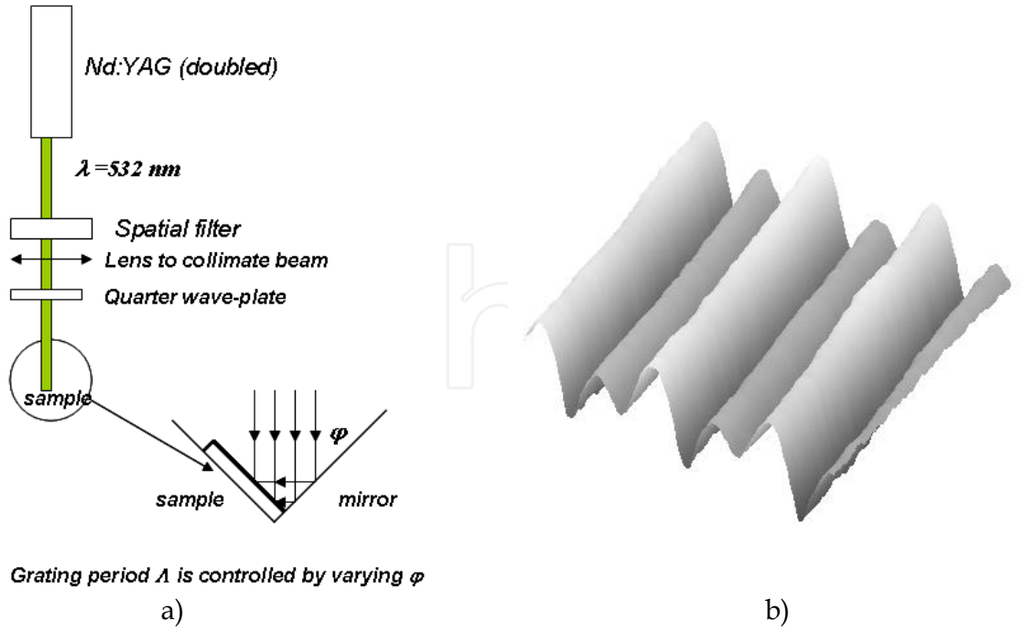

Fig. 15. a) Experimental set-up to produce corrugated metallic grating. b) Atomic force microscope image of a double metallic grating. Pitches here are 700 and 375 nm with their respective depths of 19± 1 nm and 7.0±0.5 nm.

nm thick gold film by sputter. The surface profile s(x) shown in the atomic force microscope image in Figure 15b can be represented as

$$s(x) = h_1 \sin(K_1 x) + h_2 \sin(K_2 x + \phi_2) \tag{61}$$

where x is the spatial coordinate, h_1 and h_2 are the amplitudes of the two harmonic components, and ϕ_2 is their relative phase.

4. Conclusion

The matrix formalism was shown to be efficient to predict the reflectance curves of both uniform films and periodic corrugated surfaces. It was shown in this chapter that the reflectance derived from the matrix formalism allows precise determinations of refractive indices and thickness when it is fitted to experimental data points. The principle to determine a good fit from the minimization of the sum of squares was presented in some details. The application of the sum of squares in more complex structures involving transparent overlaying films were also introduced along with waveguide modes. It was also shown that the matrix formalism can be used in numerical techniques and can be applied to periodic gratings to predict diffraction efficiencies. Systems of metallic periodic gratings were discussed and it was shown that photonic bandgap can be produced by superposition of two inscribed corrugated surface on an azopolymer film. The modulated films were made by holographic technique to write surface relief structures. One grating is written to have a spacing vector K_2 to generate a bandgap in the SP dispersion curve. A second grating with grating spacing vector K_1 is superimposed and allows the coupling of the incident light to generate the SP itself.

5. References

Barnes, W.L., Priest, T.W., Kitson, S.C. & Sambles, J.R. (1996). Physical origin of photonic energy gaps in the propagation of surface plasmons on gratings, *Phys Rev B* , Vol. 54, No. 9 (1 September 1996), pp. 6227-6244, ISSN 1098-0121

Barnes, W.L., Dereux, A. & Ebbesen, T.W. (2003). Surface plasmon sub wavelength optics, *Nature*, Vol. 424, No. 6950, (14 August 2003), pp. 824-830, ISSN 0028-0836.

Born, M. & Wolf, E. (1980). *Principles of Optics* (6th Ed.), Cambridge University Press, ISBN 0 521 63921 2, Cambridge, UK.

Ebbesen, T.W., Lezec, H.J., Ghaemi, H.F., Thio, T. & Wolff, P.A. (1998). Extraordinary optical transmission through sub wavelength hole arrays, *Nature* , Vol. 391, No. 6668, (February 12 1998), pp. 667-669, ISSN 0028-0836.

Gallatin, G.M. (1987). Properties and applications of layered grating resonances, in Applications and Theory of Periodic Structures, Diffraction Gratings, and Moiré Phenomena III, *Proc. SPIE,* Vol. 815, pp.158-167, ISBN 9780892528509.

Lalanne, P. & Morris, G.M. (1996). Highly improved convergence of the coupled-wave method for TM polarization, *J Opt Soc Am A,* Vol. 13, No.4, (April 1st 1996), pp. 779-784, ISSN 1084-7529.

Lenaerts, C., Michel, F., Tilkens, B., Lion, Y. & Renotte, Y. (2005). High transmission efficiency for surface plasmon resonance by use of a dielectric grating, *Appl Opt*, Vol. 44, No.28, (October 1st 2005), pp. 6017-6022, ISSN 1559-128X.

Lévesque, L., Paton B.E. & Payne S.H. (1994). Precise thickness and refractive index determination of polyimide films using attenuated total reflection, *Appl Opt,* Vol. 33, No.34, (Dec. 1st, 1994), pp. 8036-8040, ISSN 1559-128X.

Lévesque, L. & Rochon, P. (2005). Surface plasmon photonic bandgap in azopolymer gratings sputtered with gold, *J Opt Soc Am A*, Vol. 22, No. 11, (November 1st 2005), pp. 2564-2568, ISSN 1084-7529.

Lévesque, L. (2011). Determination of thickness and optical constants of metal films from an extended ATR spectrum by using a statistical method, *Optics & Laser technology*, Vol. 43, No. 1, (February 2011), pp. 14-19, ISSN 0030-3992.

Li, L. & Haggans, C.W. (1993). Convergence of the coupled-wave method for metallic lamellar diffraction gratings, *J Opt Soc Am A*, Vol. 10, No. 6, (June 1st 1993) , pp. 1184-1189, ISSN 1084-7529.

Magnusson, R. & Wang, S.S. (1992). New principle for optical filters, *Appl Phys Lett*, Vol. 61, No. 9, (August 31 1992), pp. 1022-1024, ISSN 003-6951.

Moharam, M.G. & Gaylord, T.K. (1981). Rigorous coupled-wave analysis of planar-grating diffraction, *J Opt Soc Am* (1917-1983), Vol. 71, No. 7, (July 1st 1981), pp. 811-818, ISSN 0030-3941.

Moharam, M.G., Grann, E.B., Pommet D.A. & Gaylord T.K. (1995). Formulation for stable and efficient implementation of the rigorous coupled-wave analysis of binary gratings, *J Opt Soc Am A*, Vol. 12, No.12, (May 1st 1995), pp. 1068-1076, ISSN 1084-7529.

Pai, D.M. & Awada, K.A. (1991). Analysis of dielectric gratings of arbitrary profiles and thicknesses, *J Opt Soc Am A*, Vol. 8, No. pp.755-762, ISSN 1084-7529.

Park, S., Lee, G., Song, S.H., Oh, C.H. & Kim, P.S. (2003). Resonant coupling of surface plasmons to radiation modes by use of dielectric gratings, *Opt Lett* , Vol. 28,No. 20, (October 15th 2003), pp. 1870-1872, ISSN 0146-9592.

Raether, H. (1988). *Surface Plasmons on Smooth and Rough Surfaces and on Gratings*, Springler-Verlag, ISBN 3-540-17363-3, Berlin, Germany.

Roberston, WM. & Fullerton E. (1989). Reexamination of surface-plasma-wave technique for determining the dielectric constant and thickness of metal films, *J Opt Soc Am B,* Vol. 6, No. 8, (August 1st 1989), pp. 1584-1589, ISSN 0740-3224.

Sheng, P., Stepleman, R.S. and Sanda, P.N. (1982). Exact eigenfunctions for square-wave gratings: Application to diffraction and surface-plasmon calculations, *Phys Rev B,* Vol. 26, No. 6, (15 September 1982) pp. 2907-2916, ISSN 1098-0121.

Tibuleac, S. & Magnusson, R. (1997). Reflection and transmission guided-mode resonance filters, *J Opt Soc Am A,* Vol. 14, No. 7, (July 1st, 1997) , pp. 1617-1626, ISSN 1084-7529.

Wang, S.S, Magnusson, R., Bagby, J.S., & Moharam, M.G. (1990). Guided-mode resonances in planar dielectric-layer diffraction gratings, *J Opt Soc Am A*, Vol. 7, No.8, (August 1st, 1990), pp.1470-1474, ISSN 1084-7529.

Welford, K. (1991). Surface plasmon-polaritons and their uses, *Opt Quant Elec,* Vol. 23, No. 1, (January 1991), pp.1-27, ISSN 0036-8075.

Wood, R.W. (1902). Remarkable spectrum from a diffraction grating, Philos Mag , Vol. 4, No. 21, (September 1902), pp. 396-402, ISSN 1941-5990.

Ye, Y.H. & Zhang, J.Y. (2004) . Middle-infrared transmission enhancement through periodically perforated metal films, *Appl Phys Lett* , Vol. 84, No.16, (April 19th,2004), pp. 2977-2979 , ISSN 003-6951.

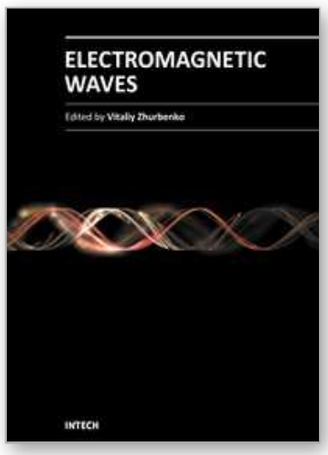

Electromagnetic Waves

Edited by Prof. Vitaliy Zhurbenko

ISBN 978-953-307-304-0
Hard cover, 510 pages
Publisher InTech
Published online 21, June, 2011
Published in print edition June, 2011

This book is dedicated to various aspects of electromagnetic wave theory and its applications in science and technology. The covered topics include the fundamental physics of electromagnetic waves, theory of electromagnetic wave propagation and scattering, methods of computational analysis, material characterization, electromagnetic properties of plasma, analysis and applications of periodic structures and waveguide components, and finally, the biological effects and medical applications of electromagnetic fields.

InTech Europe
University Campus STeP Ri
Slavka Krautzeka 83/A
51000 Rijeka, Croatia
Phone: +385 (51) 770 447
Fax: +385 (51) 686 166
www.intechopen.com

InTech China
Unit 405, Office Block, Hotel Equatorial Shanghai
No.65, Yan An Road (West), Shanghai, 200040, China
中国上海市延安西路65号上海国际贵都大饭店办公楼405单元
Phone: +86-21-62489820
Fax: +86-21-62489821

IntechOpen